Electronic Supplementary Material (ESI) for Journal of Materials Chemistry A.
This journal is © The Royal Society of Chemistry 2022

Electronic Supplementary Information

Hybridization cage-confinement pyrolysis strategy to ultrasmall Ni_3Fe alloy coated with N-doped carbon nanotubes as bifunctional oxygen electrocatalysts for Zn-air batteries

Qi Yan, Xinde Duan, Yang Liu, Fayuan Ge and Hegen Zheng*

State Key Laboratory of Coordination Chemistry, School of Chemistry and Chemical Engineering, Collaborative Innovation Center of Advanced Microstructures, Nanjing University, Nanjing 210023, P. R. China.

*Corresponding authors. E-mail: zhenghg@nju.edu.cn (Hegen. Zheng)

Experimental section

Material Characterization

Powder X-ray diffraction (P-XRD) measurements were performed on a Bruker D8 Advance X-ray diffractometer using Cu Kα radiation (λ = 1.5406 Å). Scanning electron microscope (SEM) was carried on a S-4800. Transmission electron microscope (TEM) and high-resolution transmission electron microscope (HR-TEM) were collected on a JEOL JEM-2800 microscope at a high voltage of 200 kV with a STEM unit. Thermogravimetric analysis (TGA) was performed on a STA449F3 thermoanalyzer under N_2 gas flow. Raman spectra were recorded on a Invia Raman spectrometer using a 633 nm laser. X-ray photoelectron spectra (XPS) analysis was carried out on a PHI-5000 Versa Probe XPS system. Brunauer-Emmett-Teller (BET) specific surface areas were measured by N_2 physisorption on a Micromeritics ASAP 2050 system.

Electrochemical measurements

The ORR and OER activities were evaluated by a electrochemical workstation (CHI 760E, Shanghai, Chenghua) in a standard three-electrode setup in 0.1 M KOH. A rotating disk electrode (RDE) can be used as the working electrode, Hg/Hg_2Cl_2 (KCl saturated) electrode and platinum electrode can serve as the reference electrode and counter electrode, respectively. All measured potentials are converted to reversible hydrogen electrode potential (E_{RHE}) using following Nernst equation: $E_{RHE} = E_{Hg_2Cl_2} + 0.2415 + 0.059pH$. The catalyst ink was prepared by ultrasonically dispersing the mixture of catalyst (5 mg), ethanol/H_2O solution (960 μL, 1/1, V/V), and Nafion (5 wt%, 40 μL) for 30 min. The catalyst dispersion (10 μL) was uniformly dropped onto a glassy carbon RDE (4 mm in diameter) and dried at room temperature.

For ORR test, cyclic voltammograms (CV) measurements were performed at a scan rate of 10 mV s^{-1} in O_2- and N_2-saturated 0.1 M KOH solution, while the linear sweeping voltammetry (LSV) was tested at a rotating rate ranging from 400 to 1600 rpm with a scan rate of 10 mV s^{-1}.

Rotating ring-disk electrode (RRDE) measurement was performed to further verify electron transfer number (*n*) and the production of peroxide yields (HO_2^-%) via following equations (S1-S2):

$$n = 4 \times \frac{I_d}{I_d + I_r/N} \quad \text{(S1)}$$

$$HO_2^- \% = 200 \times \frac{I_r/N}{I_d + I_r/N} \quad \text{(S2)}$$

Where I_d and I_r represent disk and ring current, respectively, and *N* represents the collection efficiency of the Pt ring (0.37).

For OER tests, the LSV curve was recorded in N_2-saturated 0.1 M KOH solution at a rotation speed of 1600 rpm at the scan rate of 2 mV s^{-1} with *iR*-compensation. The stability tests for OER were carried out by current versus time (i-t) chronoamperometric response at 1.6 V (*vs*. RHE) for 20000 s. The electrochemical surface areas (ECSA) can be estimated according to the double-layer capacitance (C_{dl}) values by recording cyclic voltammetry (CV) curves at different scan rates of 20, 40, 60, 80, 100, mV s^{-1} from 0.96 to 1.06 V (*vs.* RHE).

Zn-air battery assembly

For liquid Zn-air battery, firstly, above Ni_3Fe-NCNTs-800 ink was dropped onto a Ni foam with a loading amount of 0.5 mg cm^{-2} and dried at room temperature. Secondly, Zn powder was used as anode, Ni foam-supported catalyst layer and air-diffusion layer served as air cathode, and 6 M KOH or 6 M KOH + 0.2 M $Zn(CH_3COO)_2$ was used as the electrolyte for primary or rechargeable ZABs. Battery tests were conducted on a LAND CT2001A battery test system. For

comparison, commercial Pt/C or Pt/C + RuO_2 (mass ratio is 1:1) with same loading mass to Ni_3Fe-NCNTs-800 was used as a reference ZAB.

For all-solid-state Zn-air battery, the PVA-KOH gel electrolyte was prepared as follows: 5 g of polyvinyl alcohol (PVA) (MW 14500, Aladdin) was dissolved in 20 mL of deionized water under stirring at 95℃ for 30 min, then 5 mL of 18 M KOH+2.5 mM $Zn(CH_3COO)_2$ solution was poured into above mixture solution under stirring at 95℃ for another 30 min. The resulting transparent sol was cast into watch glasses to form a polymer film (2 mm thickness). Subsequently, the film was freezed in the refrigerator overnight and then thawed at room temperature. Then the PVA-KOH gel (2 cm × 2 cm) was put into the inner side of the zinc foil (0.2 mm thickness), and the CoFe@NC/KB-800 catalyst ink was dripped onto the PVA-KOH film with the load of 1mg cm^{-2} and dried at room temperature. Nickel foam (2 cm × 2 cm) was used as the current collector.

Theory Calculations

Our calculations were performed based on DFT implemented in the QUANTUM-ESPRESSO package.[1] Structural relaxation using spin-polarized scalar relativistic ultrasoft pseudopotentials and an exchange correlation functional in the form of a Perdew-Burke Ernzerhof functional with the van der Waals interaction by the empirical dispersion correction. Vacuum regions of at least 20 Å in vertical directions, were applied to avoid unphysical teractions between periodic images. All calculations were conducted with a plane wave cutoff of 60 rydberg and a 3 × 5 × 1 Monkhorst-Pack k-grid for the Brillouin zone, which are sufficient to ensure convergence.[2] Geometry optimization was performed using a quasi-Newton algorithm. A total energy convergence of 1.4×10^{-4} eV and residual forces below 0.02 eV $Å^{-1}$ were achieved. The most acceptable pathway for ORR is a 4-electron transfer process, accompanied by the break of O-O bond and the formation of O-H bond, and the proposed mechanism is as follows (S3-S6):

$$* + O_2 + H_2O + e^- \rightarrow OOH* + OH^- \quad \text{(S3)}$$

$$OOH* + e^- \rightarrow O* + OH^- \quad \text{(S4)}$$

$$O* + H_2O + e^- \rightarrow OH* + OH^- \quad \text{(S5)}$$

$$OH* + e^- \rightarrow * + OH^- \quad \text{(S6)}$$

Here, * is the active sites on the surface of catalysts, and OOH*, O*, OH* are intermediates.

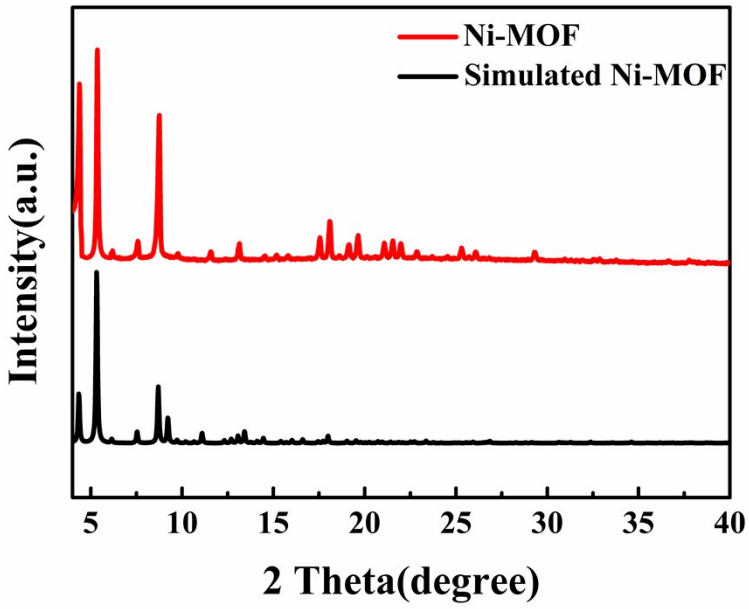

Fig. S1 PXRD patterns of simulated and Ni-MOF.

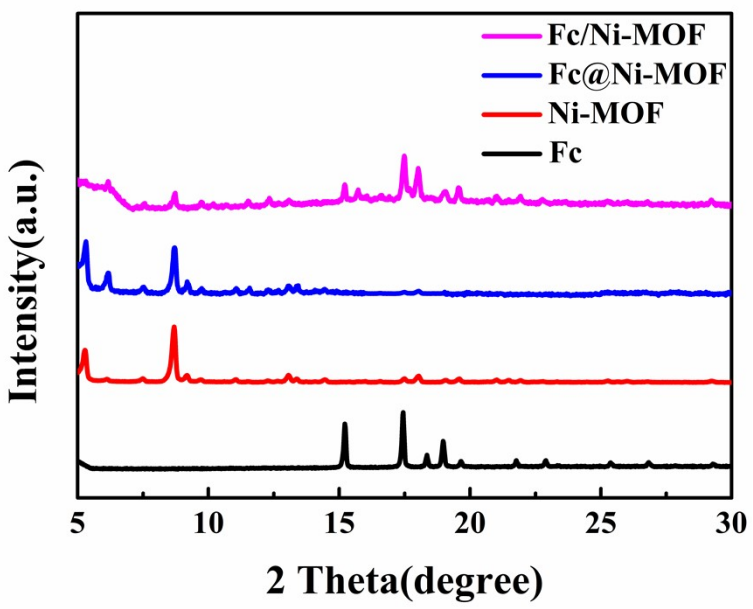

Fig. S2 PXRD patterns of Fc@Ni-MOFand Fc/Ni-MOF.

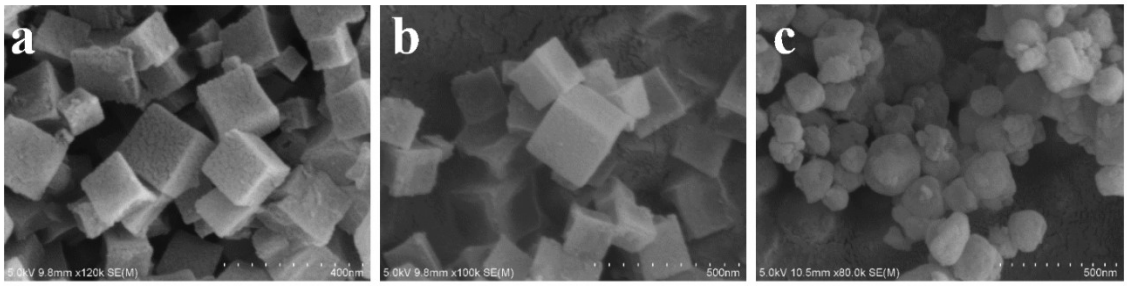

Fig. S3 SEM images of (a) Ni-MOF, (b) Fc@Ni-MOF and (c) Fc/Ni-MOF.

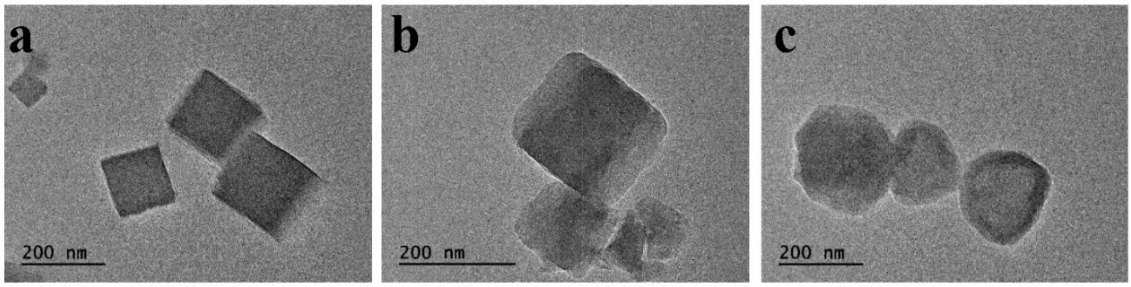

Fig. S4 TEM images of (a) Ni-MOF, (b) Fc@Ni-MOF and (c) Fc/Ni-MOF.

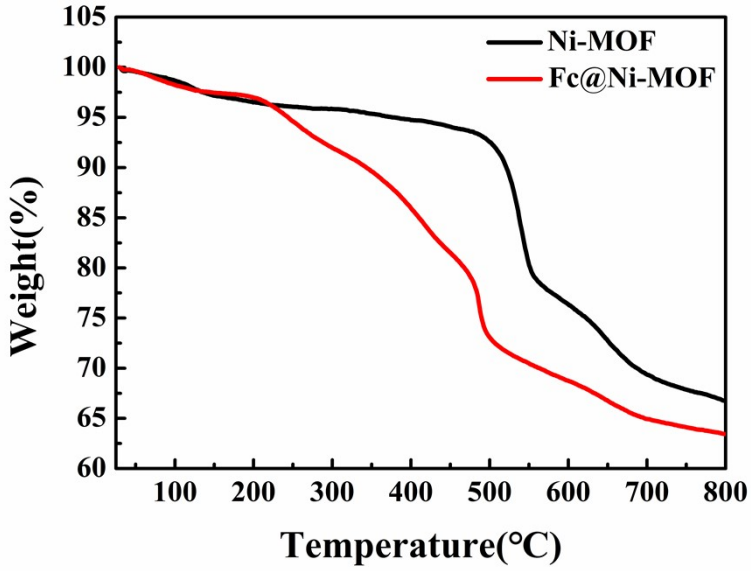

Fig. S5 TGA diagrams of Ni-MOF and Fc@Ni-MOF.

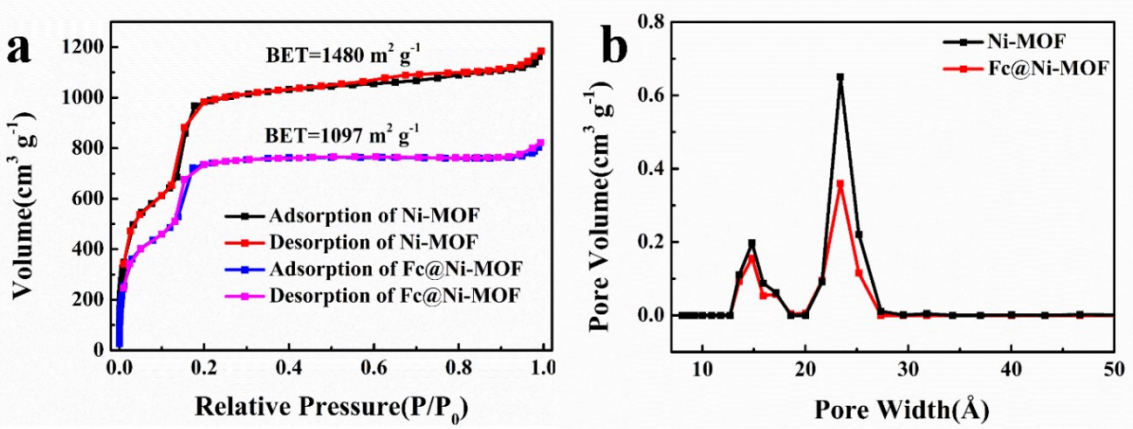

Fig. S6 (a) N_2 adsorption-desorption isotherms and (b) related pore size distributions for Ni-MOF and Fc@Ni-MOF.

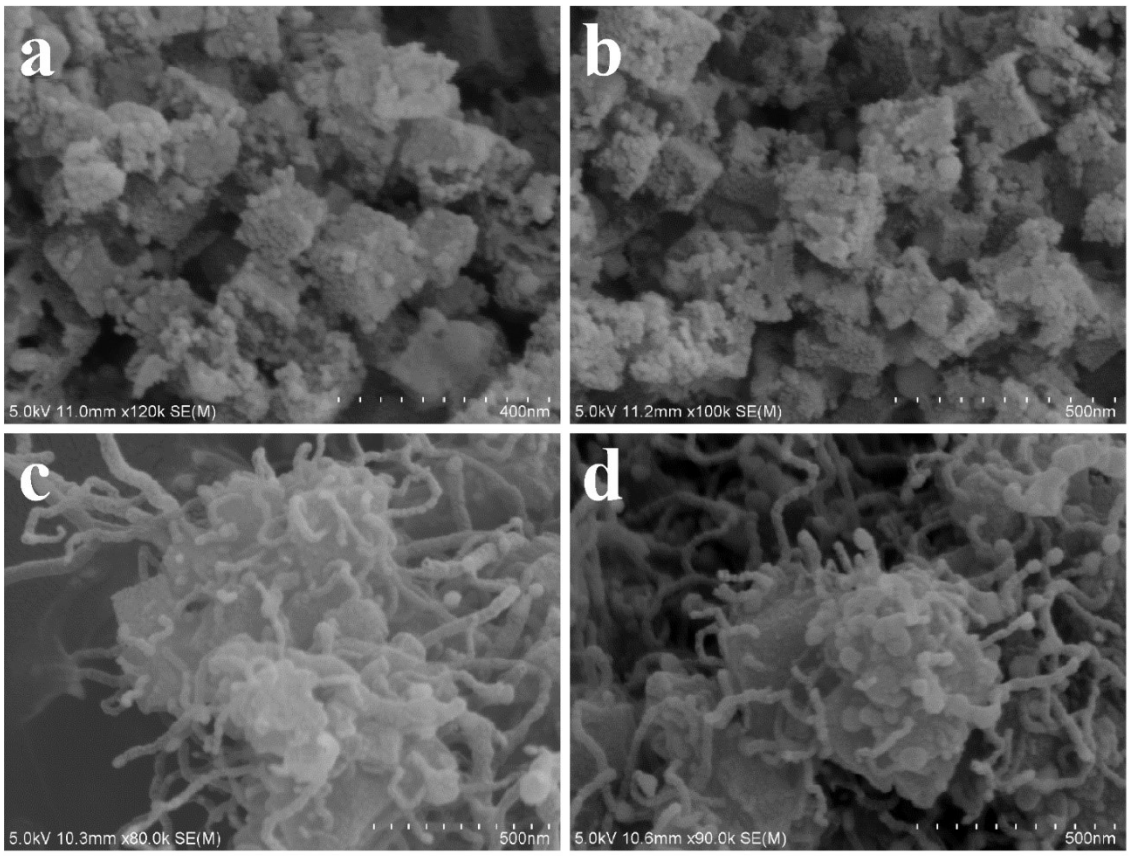

Fig. S7 SEM images of (a) Ni-NC, (b) Ni_3Fe-NC, (c) Ni_3Fe-NCNTs-700 and (d) Ni_3Fe-NCNTs-900.

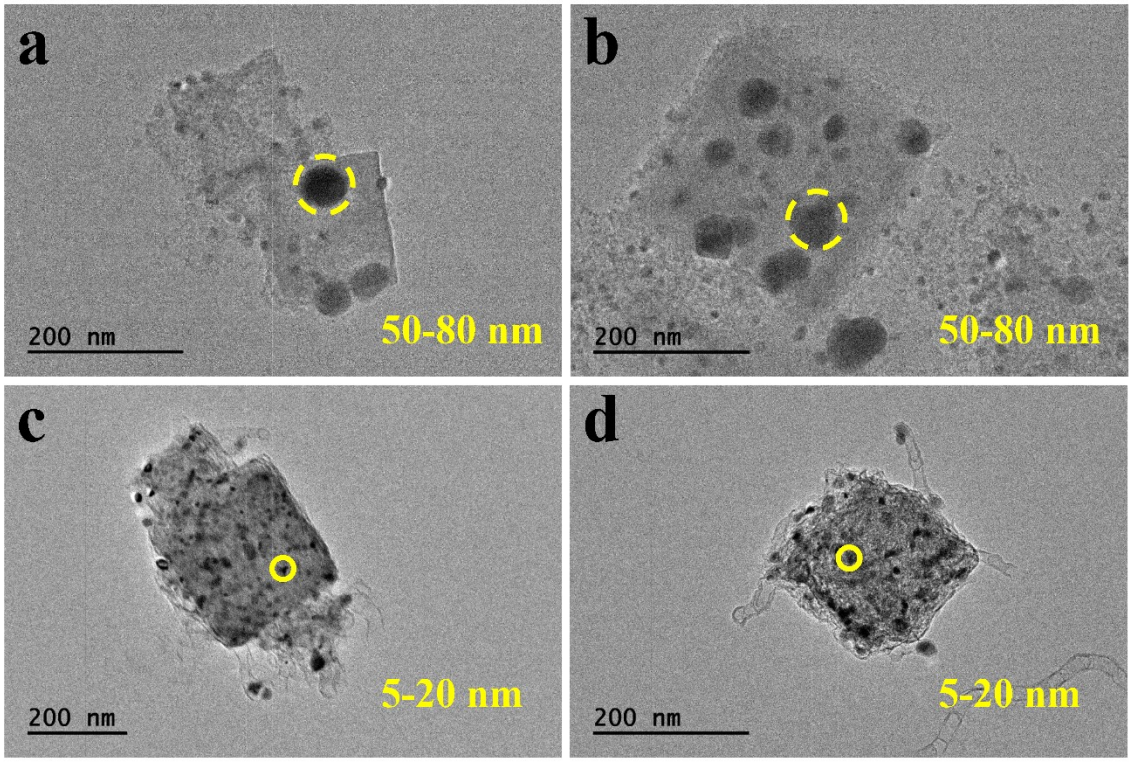

Fig. S8 TEM images of (a) Ni-NC, (b) Ni_3Fe-NC, (c) Ni_3Fe-NCNTs-700 and (d) Ni_3Fe-NCNTs-900.

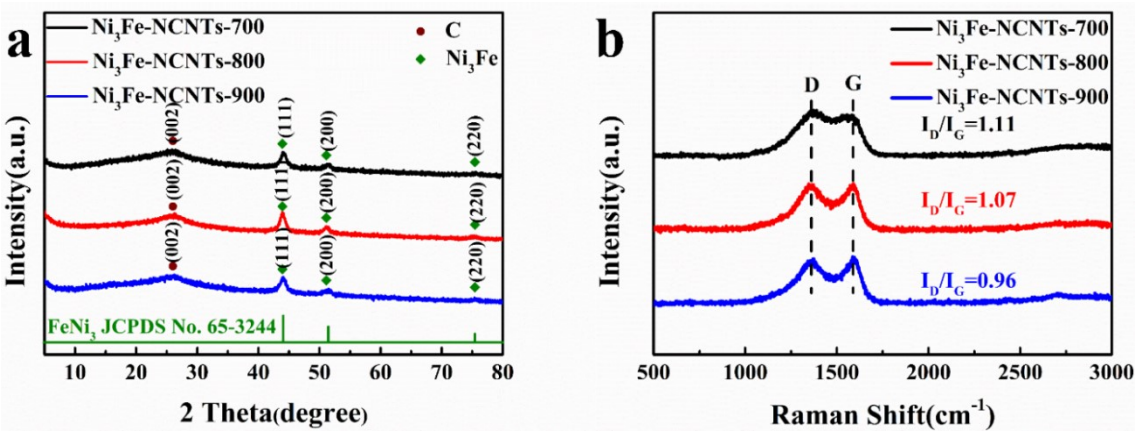

Fig. S9 (a) PXRD and (b) Raman patterns of Ni_3Fe-NCNTs-700, Ni_3Fe–NCNTs-800 and Ni_3Fe-NCNTs-900.

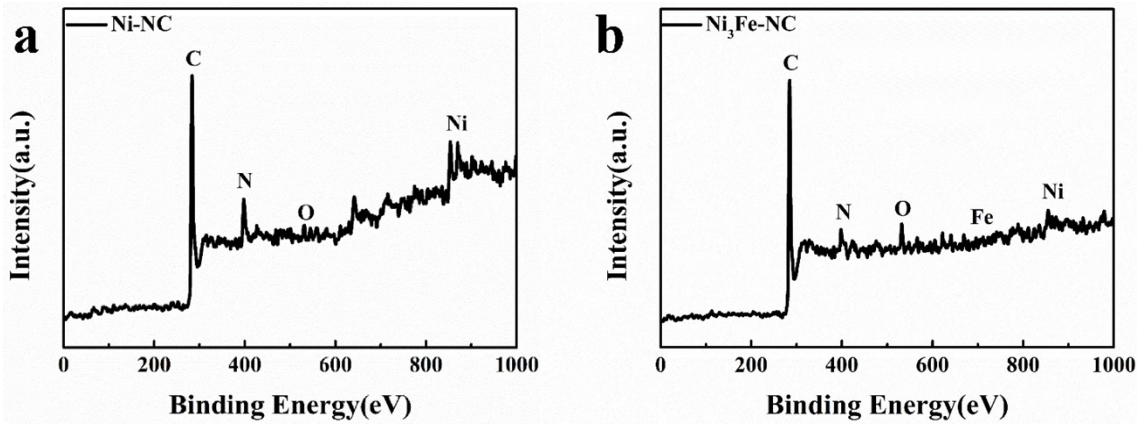

Fig. S10 XPS full spectrum of Ni-NC and Ni_3Fe-NC.

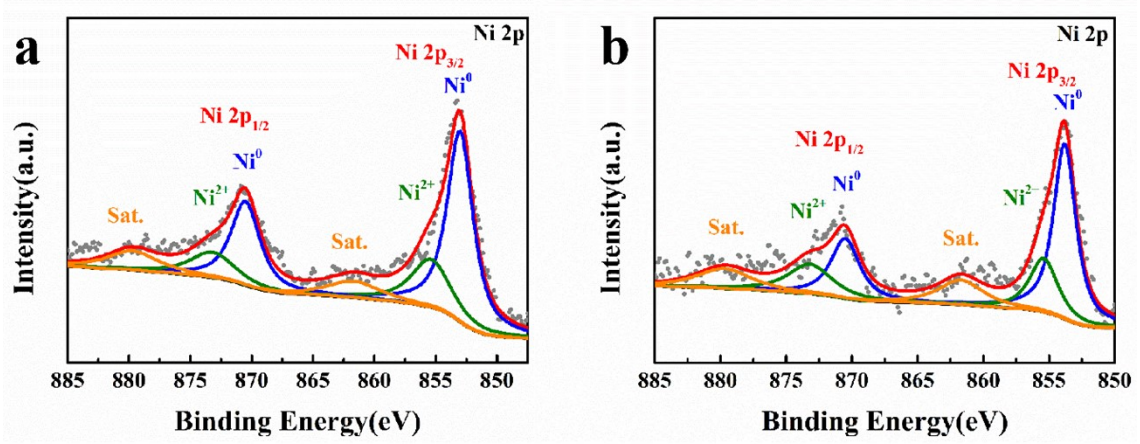

Fig. S11 Ni 2*p* high-resolution XPS spectrum of (a) Ni-NC and (b) Ni_3Fe-NC.

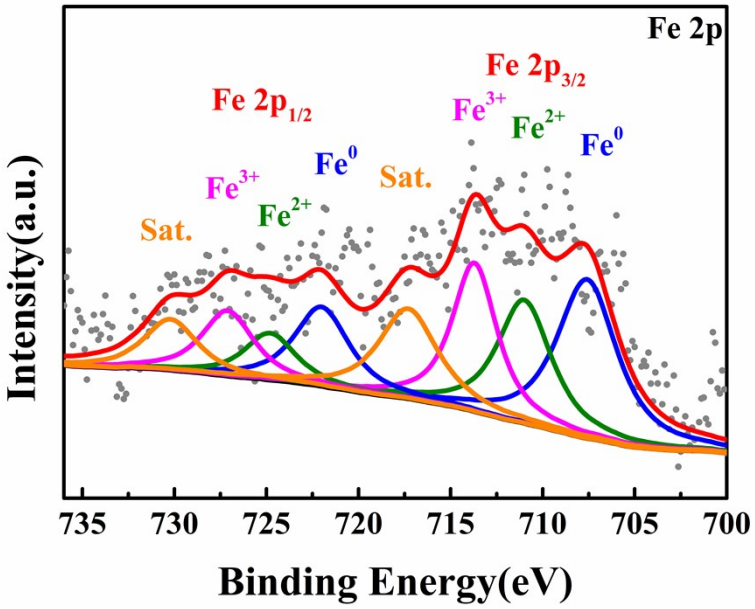

Fig. S12 Fe 2*p* high-resolution XPS spectrum of Ni_3Fe-NC.

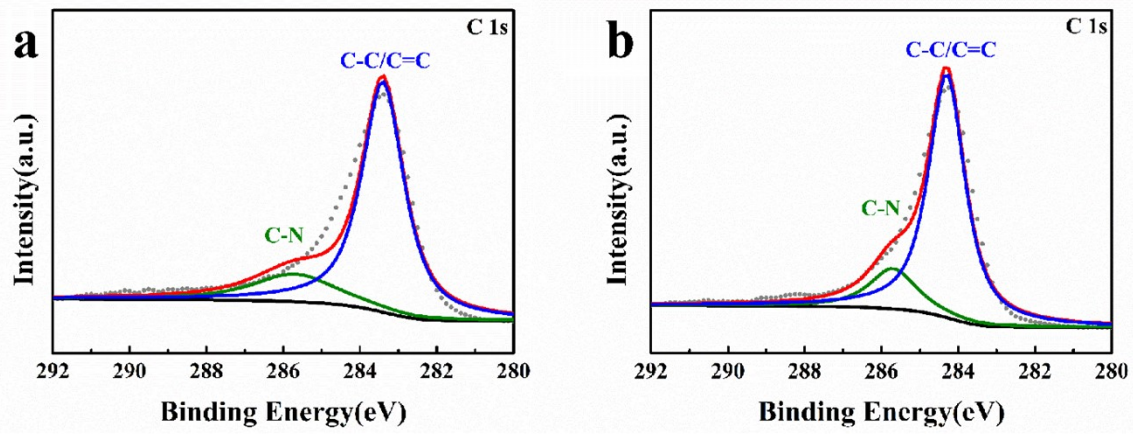

Fig. S13 C 1*s* high-resolution XPS spectrum of (a) Ni-NC and (b) Ni_3Fe-NC.

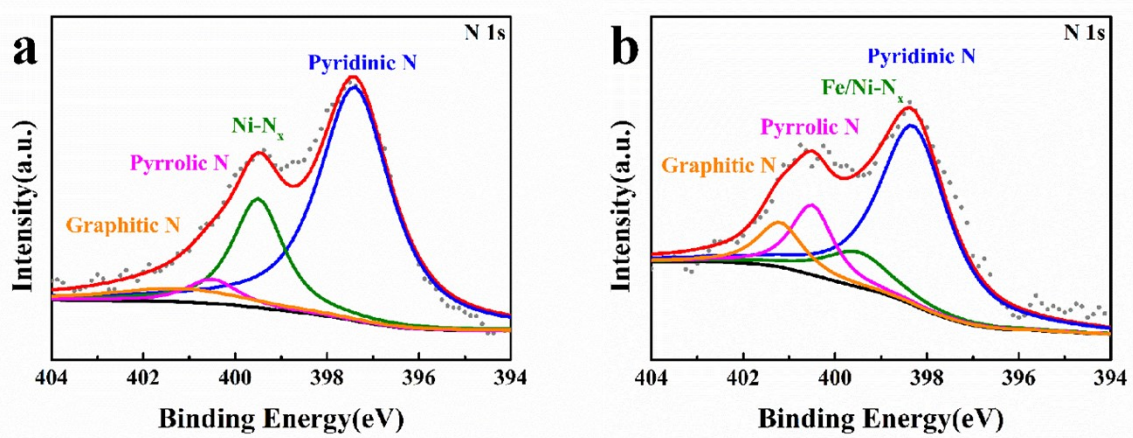

Fig. S14 N 1*s* high-resolution XPS spectrum of (a) Ni-NC and (b) Ni_3Fe-NC.

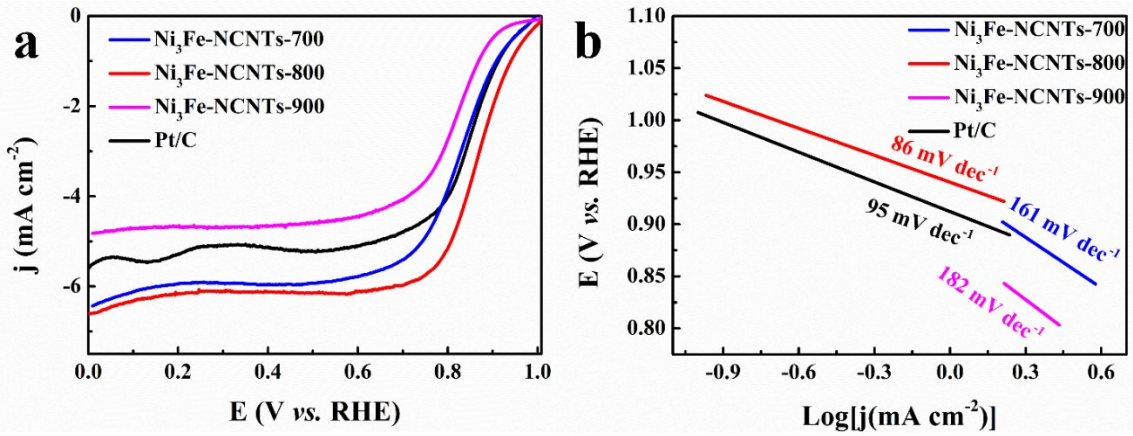

Fig. S15 (a) ORR polarization curves and (b) corresponding Tafel plots for Ni_3Fe-NCNTs-700, Ni_3Fe-NCNTs-800 and Ni_3Fe-NCNTs-900 on RDE at 1600 rpm.

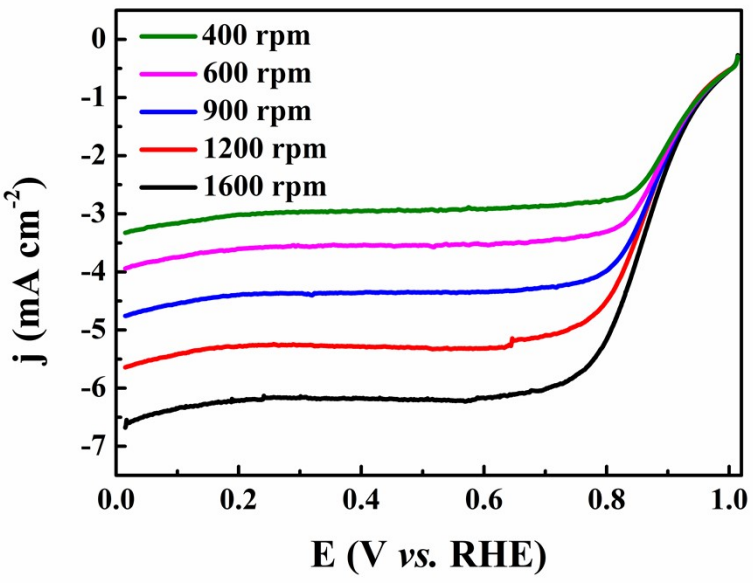

Fig. S16 LSV curves of Ni_3Fe-NCNTs-800 at various rotation speeds.

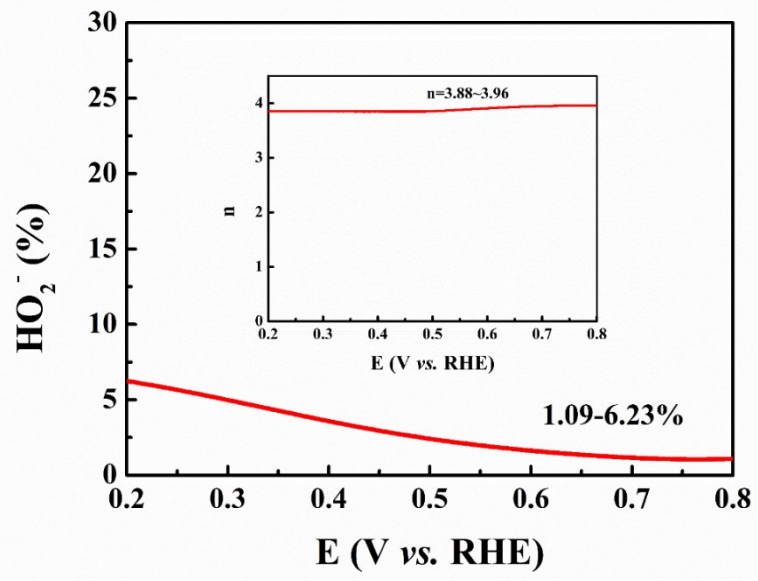

Fig. S17 H_2O_2 yield of Ni_3Fe-NCNTs-800; inset image is the electron transfer number (n).

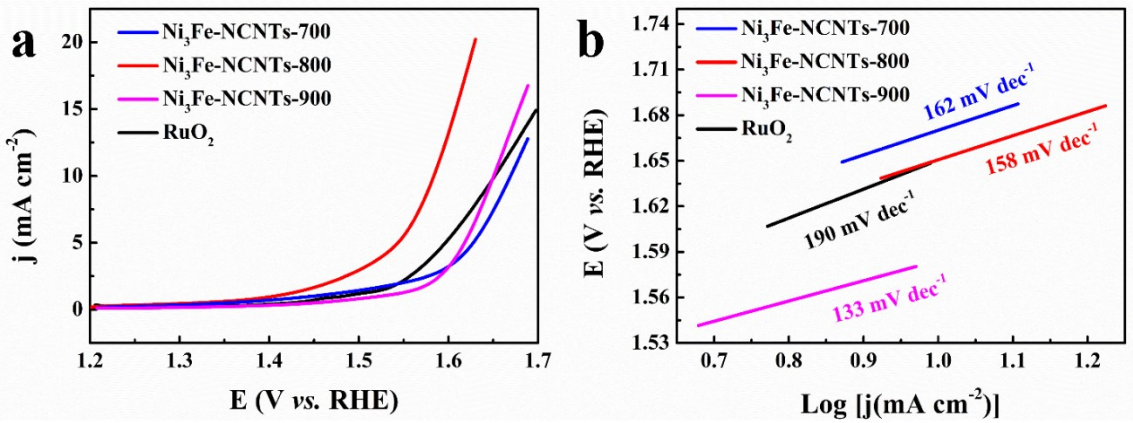

Fig. S18 (a) OER polarization curves and (b) corresponding Tafel plots for Ni_3Fe-NCNTs-700, Ni_3Fe-NCNTs-800 and Ni_3Fe-NCNTs-900 on RDE at 1600 rpm.

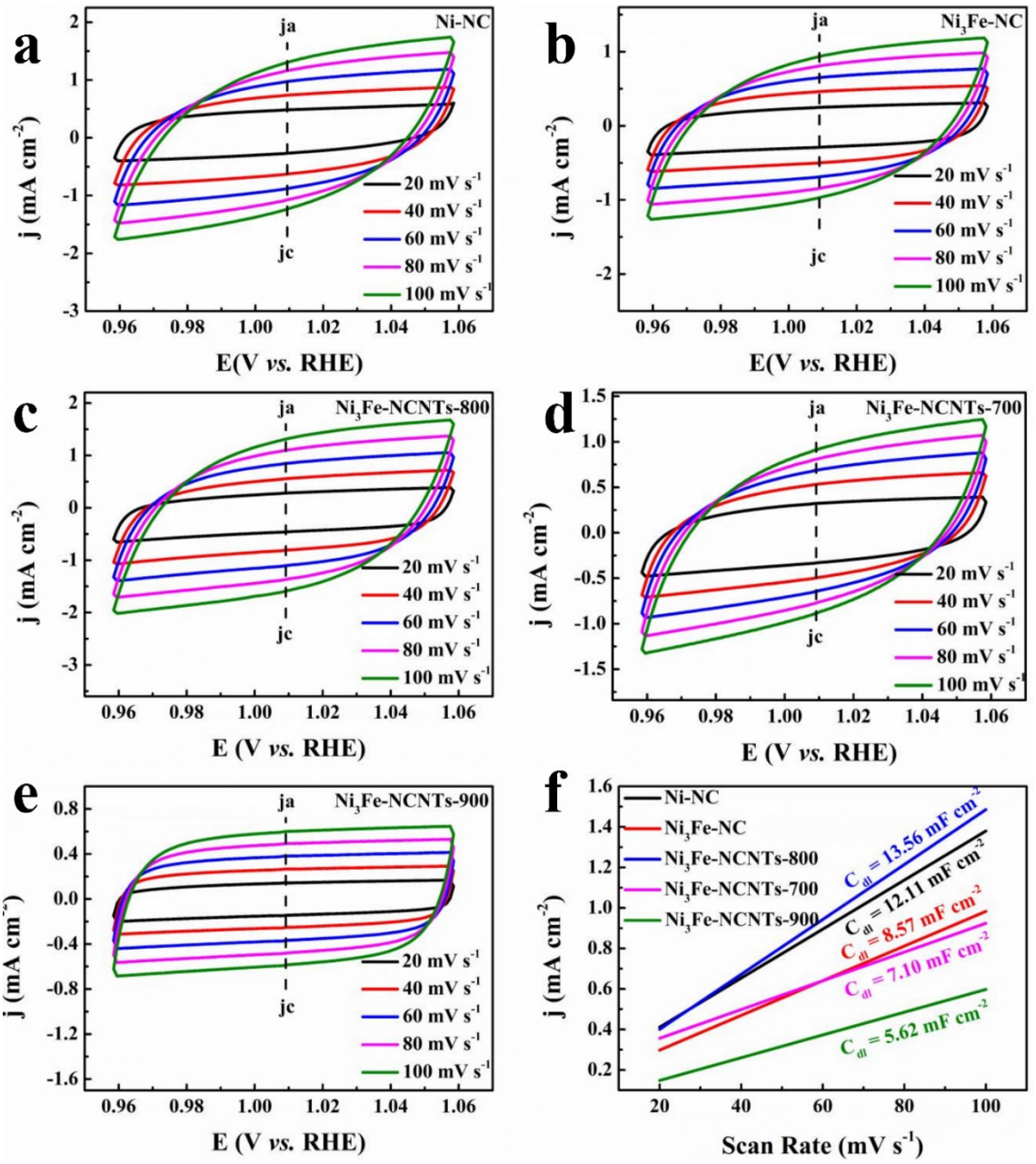

Fig. S19 (a-e) The cyclic voltammograms curves of samples in the region of 0.96-1.06 V *vs*. RHE in 0.1 M KOH. (f) The corresponding electrochemical double-layer capacitances of samples.

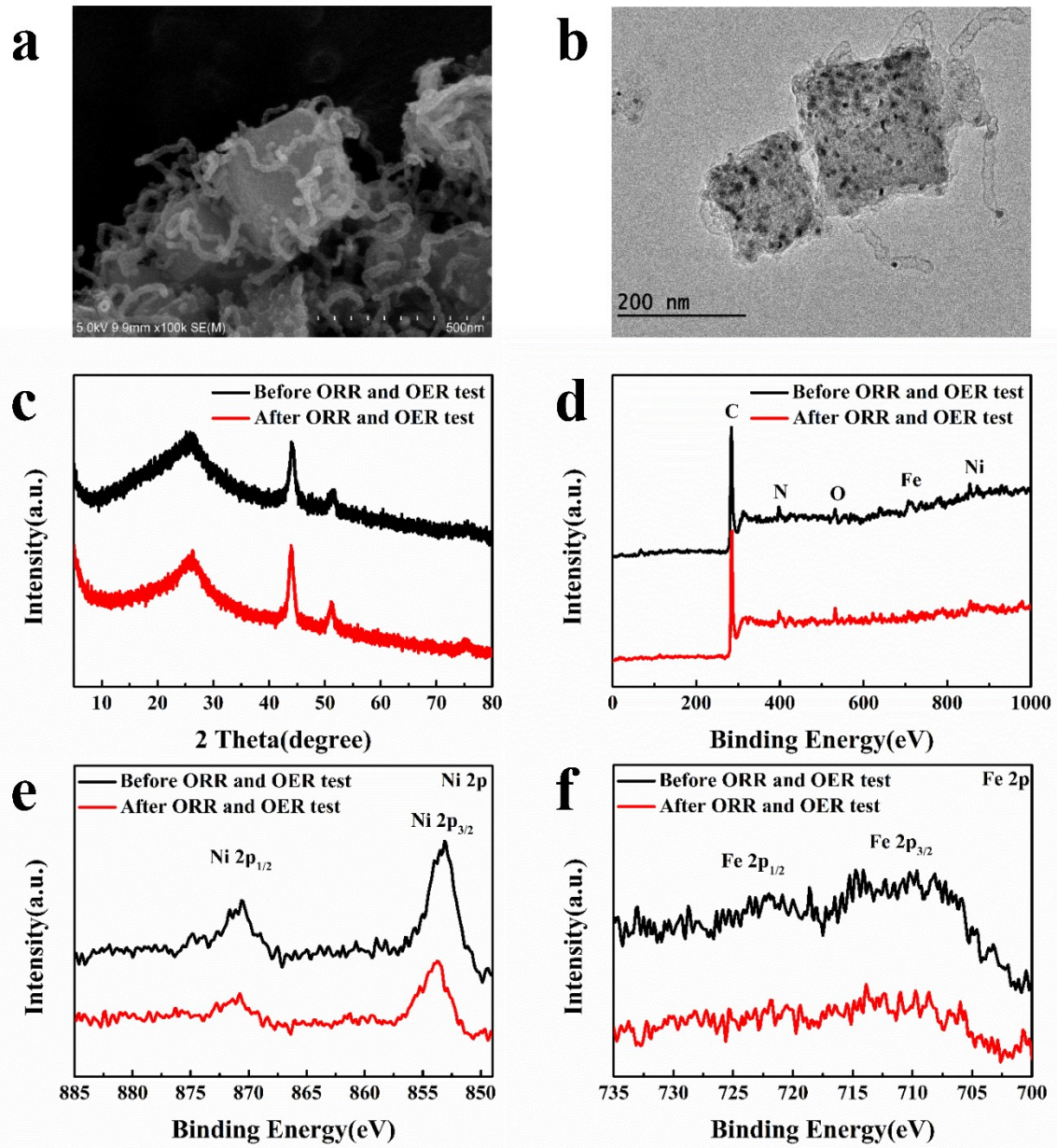

Fig. S20 (a) SEM image; (b) TEM image; (c) PXRD pattern; (d) Survey XPS spectrum; (e) Ni 2*p*; and (f) Fe 2*p* high-resolution XPS spectra of Ni_3Fe-NCNTs-800 after ORR and OER test.

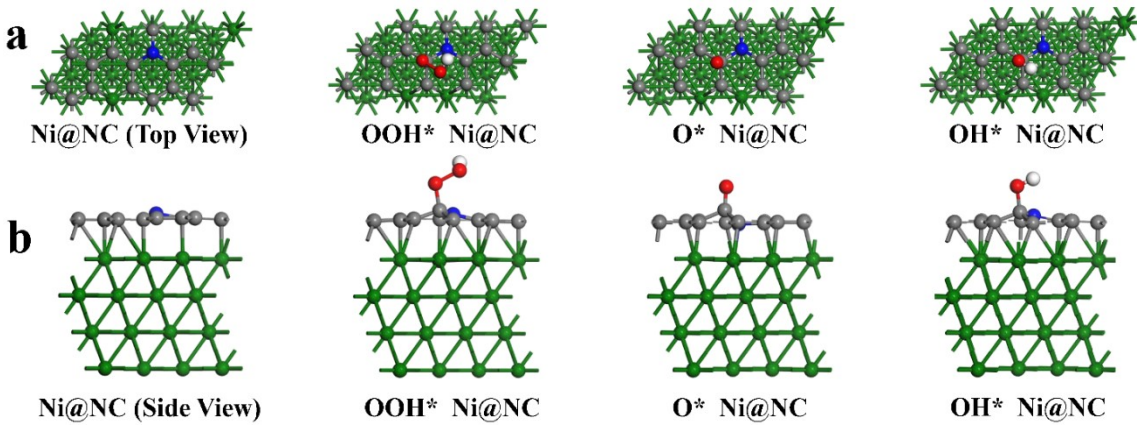

Fig. S21 Optimized configurations of intermediates (OOH*, O*, and OH*) adsorbed on Ni@NC (a) top view and (b) side view.

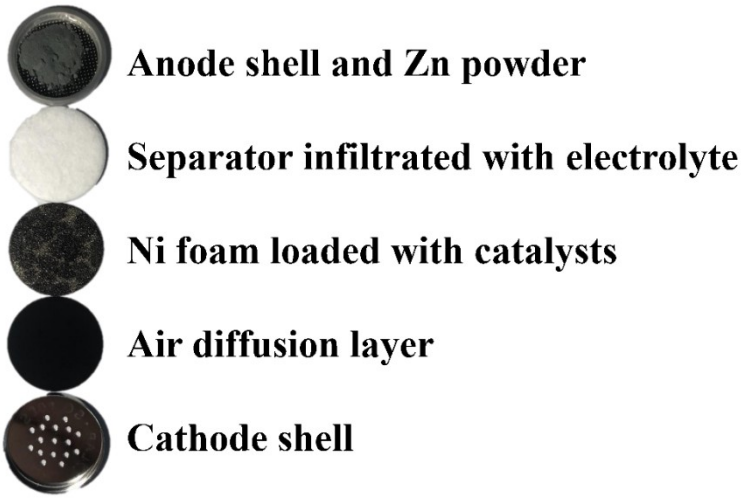

Fig. S22 Digital image of the configuration for button ZAB.

Fig. S23 Digital image of the button ZAB displaying an open circuit voltage of 1.51 V.

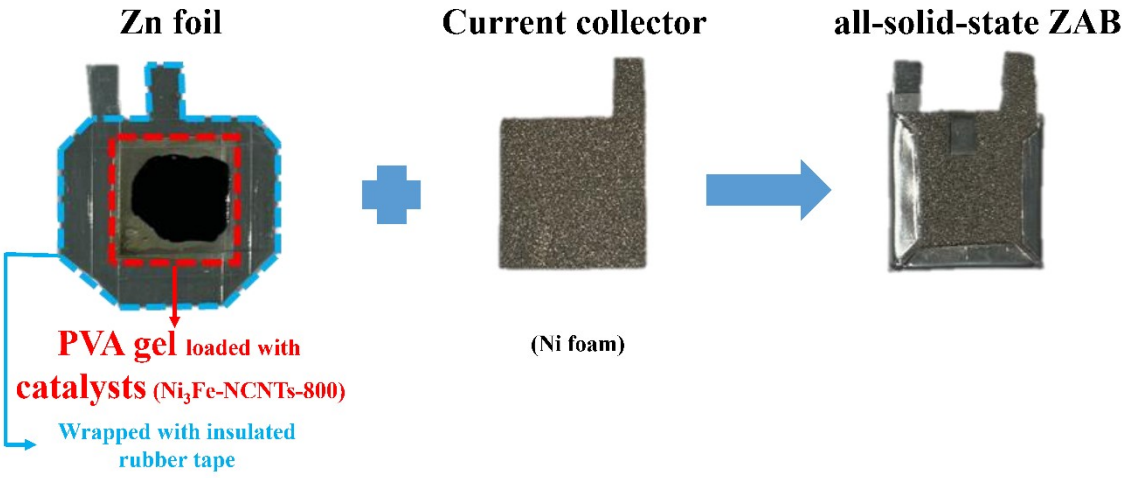

Fig. S24 Digital image of the configuration for all-solid-state ZAB.

Table S1 XPS spectra analysis for samples.

Sample	C 1s (%)	N 1s (%)	O 1s (%)	Ni 2p (%)	Fe 2p (%)
Ni-NC	84.62%	10.81%	2.82%	1.75%	--
Ni_3Fe-NC	88.20%	5.20%	5.20%	1.03%	0.37%
Ni_3Fe-NCNTs-800	85.55%	5.84%	3.04%	3.48%	1.19%

Table S2 XPS spectra analysis of N 1s for samples.

Sample	Pyridinic N	Fe/Ni–N_x	Pyrrolic N	Graphitic N
Ni-NC	397.4 eV, 66.2%	399.5 eV, 21.7%	400.5 eV, 4.9%	401.2 eV, 7.2%
Ni_3Fe-NC	398.3 eV, 62.8%	399.5 eV, 12.1%	400.5 eV, 14.8%	401.2 eV, 10.2%
Ni_3Fe-NCNTs-800	397.7 eV, 69.4%	399.5 eV, 23.7%	400.5 eV, 4.3%	401.2 eV, 2.6%

Table S3 The ORR/OER activity comparison of Ni_3Fe-NCNTs-800 and Pt/C + RuO_2 with the state-of-the-art catalysts.

Catalyst	$E_{1/2}$	$E_{j=10}$	$\Delta E = E_{j=10} - E_{1/2}$	References
Ni_3Fe-NCNTs-800	0.862	1.583	0.721	This work
Pt/C + RuO_2	0.843	1.651	0.808	This work
CoFe@NC-SE	0.82	1.62	0.8	3
FeNi/N-CNT	0.83	1.59	0.76	4
Co-N-Cs	0.84	1.64	0.8	5
Ni-N_4/GHSs/Fe-N_4	0.83	1.62	0.79	6
NiFe@N-CFs	0.82	1.53	0.71	7
Co SANC-850	0.863	1.75	0.887	8
P-FeNi/NC@G	0.81	1.54	0.73	9
Fe/Co-CNT@MXene-8	0.85	1.59	0.74	10
hydrophobic-Co_3O_4 NSs/CC	0.73	1.59	0.86	11
YSSHs-NSC-Co_9S_8	0.83	1.58	0.75	12
IOSHs-NSC-Co_9S_8	0.82	1.64	0.82	13
NdDCF-OIM/Co	0.83	1.60	0.77	14

Table S4 The ΔE_{ads} and ΔG_{ads} of oxygenated intermediates involved in OER and ORR processes on Ni@NC or Ni_3Fe@NC.

Intermediates	Ni_3Fe@NC (eV)	Ni@NC (eV)
ΔE_{OH*}	0.85	0.80
ΔG_{OH*}	1.13	1.07
ΔE_{O*}	1.95	1.21
ΔG_{O*}	1.91	1.16
ΔE_{OOH*}	3.81	3.96
ΔG_{OOH*}	4.02	4.17

Table S5 The ZAB performances comparison of Ni_3Fe-NCNTs-800 with the state-of-the-art catalysts.

Catalyst	Open circuit potential (V)	Peak power density (mW cm^{-2})	Charge/ discharge Voltage gap (V)	Specific capacity (mAh g_{Zn}^{-1})	Stability	Ref.
Ni_3Fe-NCNTs-800	1.51	211	0.50@2 mA cm^{-2}	806	1350 cycles (225 h) at 2 mA cm^{-2}, voltage gap increased ~0.14 V	This work
CoFe@NC-SE	1.581	102	0.82@2 mA cm^{-2}	-	288 cycles (48 h) at 5 mA cm^{-2}, voltage gap increased ~0.13 V	3
FeNi/N-CNT	1.54	127	0.92@5 mA cm^{-2}	838	1200 cycles (800 h) at 5 mA cm^{-2}, voltage gap increased ~0.08 V	4
Co-N-Cs	-	128	0.7@2 mA cm^{-2}	-	600 cycles (110 h) at 2 mA cm^{-2}, voltage gap increased ~0.12 V	5
Ni-N_4/GHSs/Fe-N_4	1.45	-	0.88@10 mA cm^{-2}	777.6	600 cycles (200 h) at 10 mA cm^{-2}, roundtrip efficiency is 52.2%	6
NiFe@N-CFs	1.4	102	0.77@10 mA cm^{-2}	729	475 cycles (150 h) at 10 mA cm^{-2}, voltage gap increased ~0.11 V	7
Co SANC-850	1.48	-	0.78@10 mA cm^{-2}	860.95	44 h at 10 mA cm^{-2}, no obvious voltage change	8
P-FeNi/NC@G	1.53	159	0.73@5 mA cm^{-2}	753	144 cycles (25 h) at 5 mA cm^{-2}, voltage gap increased ~0.15 V	9
Fe/Co-CNT@MXene-8	1.41	138	0.84@10 mA cm^{-2}	759	1000 cycles (350 h) at 10 mA cm^{-2}, roundtrip efficiency is 59.0%	10

hydrophobic-Co_3O_4 NSs/CC	1.42	171	0.79@5 mA cm^{-2}	803	500 cycles at 5 mA cm^{-2}, no obvious voltage change	11
PAA-Fe^{3+}-CS/NH_4Cl	1.45	55.4	1.56@10 mA cm^{-2}	719	360 cycles (120 h) at 5 mA cm^{-2}, no obvious voltage change	12
IOSHs-NSC-Co_9S_8	1.497	133	0.872@10 mA cm^{-2}	738	240 cycles (80 h) at 10 mA cm^{-2}, voltage gap increased ~0.29 V	13
NdDCF-OIM/Co-800	1.346	167	0.79@2 mA cm^{-2}	749	165 cycles (55 h) at 2 mA cm^{-2}, voltage gap increased ~0.03 V	14

References

1. P. Giannozzi, S. Baroni, N. Bonini, M. Calandra, R. Car, C. Cavazzoni, D. Ceresoli, G. L. Chiarotti, M. Cococcioni, I. Dabo, A. Dal Corso, S. de Gironcoli, S. Fabris, G. Fratesi, R. Gebauer, U. Gerstmann, C. Gougoussis, A. Kokalj, M. Lazzeri, L. Martin-Samos, N. Marzari, F. Mauri, R. Mazzarello, S. Paolini, A. Pasquarello, L. Paulatto, C. Sbraccia, S. Scandolo, G. Sclauzero, A. P. Seitsonen, A. Smogunov, P. Umari and R. M. Wentzcovitch, *J. Phys. Condens. Matter.*, 2009, **21**, 395502.
2. S. Froyen, *Phys. Rev. B Condens. Matter.*, 1989, **39**, 3168-3172.
3. A. Samanta and C. R. Raj, *J. Power Sources*, 2020, **455**, 227975.
4. Z. Li, J. Yang, X. Ge, Y.-P. Deng, G. Jiang, H. Li, G. Sun, W. Liu, Y. Zheng, H. Dou, H. Jiao, J. Zhu, N. Li, Y. Hu, M. Feng and Z. Chen, *Nano Energy*, 2021, **89**, 106314.
5. S. Chen, L. Ma, S. Wu, S. Wang, Z. Li, A. A. Emmanuel, M. R. Huqe, C. Zhi and J. A. Zapien, *Adv. Funct. Mater.*, 2020, **30**, 1908945.
6. J. Chen, H. Li, C. Fan, Q. Meng, Y. Tang, X. Qiu, G. Fu and T. Ma, *Adv Mater*, 2020, **32**, 2003134.
7. Y. Niu, X. Teng, S. Gong and Z. Chen, *J. Mater. Chem. A*, 2020, **8**, 13725-13734.
8. Y. Wang, B. Yu, K. Liu, X. Yang, M. Liu, T.-S. Chan, X. Qiu, J. Li and W. Li, *J. Mater. Chem. A*, 2020, **8**, 2131-2139.
9. X. Yang, X. Wu, Z. Guo, Q. Li, H. Wang, C. Ke, W. Zeng, X. Qiu, Y.He, X. Liang and Y. Kim, *RSC Adv.*, 2020, **10**, 33327-33333.
10. C. Zhang, H. Dong, B. Chen, T. Jin, J. Nie and G. Ma, *Carbon*, 2021, **185**, 17-26.
11. K. Tang, H. Hu, Y. Xiong, L. Chen, J. Zhang, C. Yuan and M. Wu, *Angew. Chem. Int. Ed.*, 2022, **61**, e202202671.
12. K. Tang, J. Fu, M. Wu, T. Hua, J. Liu, L. Song and H. Hu, *Small Methods*, 2022, **6**, 2101276.
13. K. Tang, C. Yuan, Y. Xiong, H. Hu and M. Wu, *Appl. Catal. B: Environ.*, 2020, **260**, 118209.
14. J. Zhao, J. Fu, H. Hu, W. Fang, Z. Bai, W. Zhang and M. Wu, *J. Mater. Chem. A*, 2021, **9**, 5097-5110.